THE JOURNAL OF PHYSICAL CHEMISTRY A

Article

pubs.acs.org/JPCA

# Semiclassical Hybrid Approach to Condensed Phase Molecular Dynamics: Application to the $I_2Kr_{17}$ Cluster

Max Buchholz,*[,†] Christoph-Marian Goletz,[†] Frank Grossmann,[†] Burkhard Schmidt,[‡] Jan Heyda,[§] and Pavel Jungwirth[∥]

[†]Institut für Theoretische Physik, Technische Universität Dresden, 01062 Dresden, Germany

[‡]Institut für Mathematik, Freie Universität Berlin, Arnimallee 6, 14195 Berlin, Germany

[§]Institute for Soft Matter and Functional Materials, Helmholtz-Zentrum Berlin für Materialien und Energie GmbH, Hahn-Meitner-Platz 1, 14109 Berlin, Germany

[∥]Institute of Organic Chemistry and Biochemistry, Academy of Sciences of the Czech Republic, Flemingovo nam. 2, 16610 Prague 6, Czech Republic

**ABSTRACT:** We study the vibrational decoherence dynamics of an iodine molecule in a finite krypton cluster comprising the first solvation shell. A normal mode analysis allows us to successively increase the complexity of the description. For the ground state dynamics, comparison with experimental matrix results shows that already four degrees of freedom are sufficient to capture the main decoherence mechanism. For electronically excited iodine, we model the vibrational dynamics of initial Schrödinger cat-like states by the semiclassical hybrid dynamics [Grossmann, F. *J. Chem. Phys.* **2006**, *125*, 014111] and full quantum calculations, where available. Good agreement of the results is found for a reduced model with three degrees of freedom. We find non-Gaussian distortions of the bath density matrix, which is a necessary condition, if Schrödinger catlike states in the bath are to be identified. However, in contrast to the experiment [Segale, D.; et al. *J. Chem. Phys.* **2005**, *122*, 111104], we observe only incoherent superpositions of bath vibrational states.

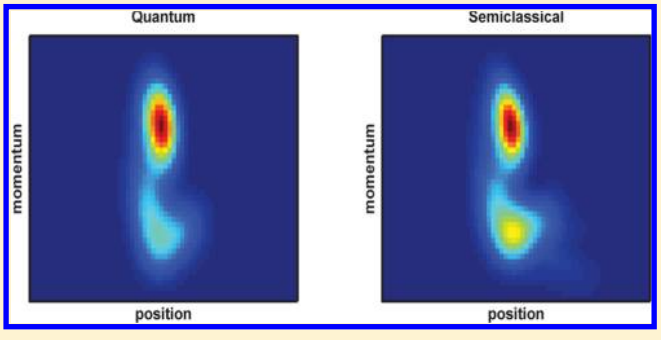


## I. INTRODUCTION

Molecular dynamics in condensed phases can often be modeled in terms of a quantum system that interacts with many surrounding bath degrees of freedom (DOFs), thereby typically experiencing rapid decoherence. In prototypical experiments in the field, the environment consists of rare gas clusters/solids/liquids.[1−3] One way to describe such systems is by mixed quantum-classical approaches that have been designed to treat part of the DOFs on a classical level to make dynamical calculations feasible. The time-resolved coherent anti-Stokes Raman spectroscopy (TRCARS) experiments by the Apkarian group on the ground state iodine molecule in a krypton matrix,[4] for example, have recently been modeled and, using a mixed quantum-classical Liouville method, two groups have been able to reach very good agreement with experimentally observed decay rates.[5,6] For a recent text book on quantum-classical methods and an extensive list of references, see refs 5 and 7. The questions of how to correctly interface quantum with classical dynamics, how to determine the initial conditions for the classical DOFs, and how to devise efficient numerical solvers,[8,9] nevertheless, leave room for a lot of debate.

Alternative approaches are based on the quantum mechanical propagator, which allows us to start the dynamics using the true quantum initial conditions and in its original form treats the dynamics of all DOFs on equal footing, although the dynamical ingredients for all DOFs are solely the solutions of Hamilton's equations. These so-called semiclassical initial value representation (IVR) methods have experienced a renaissance in the 1990s, especially in the field of theoretical (chemical) physics of atomic and molecular systems.[10−12] One of the most prominent semiclassical IVR methods was inspired by work of Heller,[13] finally devised by Herman and Kluk,[14] and studied in detail by Kay.[15,16] In principle this so-called Herman−Kluk (HK) propagator is the first term in a series representation of the full quantum propagator and by calculating higher order terms even deep tunneling may be described in terms of real-valued trajectories.[17,18] In general, however, even the semiclassical IVR method is plagued by the fact that an exceedingly large number of trajectories may be needed to converge the oscillating, possibly rapidly increasing integrand appearing in the propagator expression. Therefore, even simpler expressions have been looked for. One of them is the thawed Gaussian wave packet dynamics (TGWD)[19] of Heller. This method is based on the

**Special Issue:** Jörn Manz Festschrift

**Received:** May 25, 2012
**Revised:** July 20, 2012
**Published:** July 23, 2012

   dx.doi.org/10.1021/jp305084f | *J. Phys. Chem. A* 2012, 116, 11199−11210

propagation of a single Gaussian with time-dependent width ("thawed"), in contrast to the fixed width ("frozen") Gaussians of the HK propagator. It has been shown that the TGWD is in fact an approximation to the HK propagator if applied to a Gaussian initial state.[20,21] Another, alternative way is to use different levels of approximation to the prefactor in the Herman–Kluk propagator.[13,22−24]

The TGWD is a single trajectory method and therefore does not depend on sampling of initial conditions. For at most harmonic potential, TGWD results are exact. Thus this method might be very well suited for the description of weakly coupled environmental DOFs, whose dynamics is expected to take place near the potential minimum, where a harmonic approximation is justified. In this spirit a recently developed method[21] combines the advantages of the semiclassical IVR multitrajectory Herman–Kluk (HK)[14] method with Heller's single-trajectory (TGWD)[19] approach to apply it to typical system-bath type of situations. This semiclassical hybrid dynamics (SCHD) has later been extended to the density matrix level of description[25] and including finite temperatures.[26] These developments make the method ideally suited to be applied to a study of the decoherence dynamics of $I_2$ in a finite krypton matrix as studied experimentally in the group of Apkarian.[4] As far as possible, we will compare the semiclassical hybrid results with full quantum calculations as well as experimental results.

The paper is organized as follows: In section II the semiclassical hybrid method is reviewed. In section III we give the details of our pseudo normal mode description of $I_2$ in a krypton cluster, where we restrict the level of description of the matrix to the first solvation shell. In section IV we show full quantum results for the decoherence dynamics in the electronic ground state and compare them with experimental results. Section V deals with excited state dynamics and SCHD results are compared with full quantum ones. Our final conclusions are presented in section VI.

## II. SEMICLASSICAL HYBRID DYNAMICS

We first review the semiclassical hybrid approach[21] used in this paper. To this end, we start by sketching the semiclassical IVR of Herman and Kluk[14] and its relation to TGWD.[19] The combination of these two methods leads to the SCHD, which has been generalized for reduced density matrix dynamics in ref 25.

**A. Herman–Kluk Propagator.** A quantum mechanical wave function $\Psi(\mathbf{x},t)$ at time $t$ for a system with $N$ DOFs $\mathbf{x} \in \mathbb{R}^N$ can be obtained by applying the quantum mechanical propagator to the initial wave function $\Psi(\mathbf{x},0)$ according to

$$\Psi(\mathbf{x},t) = \int \mathrm{d}^N\mathbf{x}'\, K(\mathbf{x},t;\mathbf{x}',0)\, \Psi(\mathbf{x},0) \tag{1}$$

A semiclassical approximation to the propagator based on multiple frozen Gaussians was developed by Herman and Kluk,[14] building on previous work by Heller.[13] The corresponding propagator is given by

$$K^{\mathrm{HK}}(\mathbf{x},t;\mathbf{x}',0) = \int \frac{\mathrm{d}^N q\ \mathrm{d}^N p}{(2\pi\hbar)^N} \langle \mathbf{x}|g_\gamma(\mathbf{q}_t,\mathbf{p}_t)\rangle \times \sqrt{\det[\mathbf{h}(\mathbf{q},\mathbf{p},t)]}\, \mathrm{e}^{\mathrm{i}S/\hbar} \langle g_\gamma(\mathbf{q},\mathbf{p})|\mathbf{x}'\rangle \tag{2}$$

Its main ingredients are normalized Gaussian wave packets (GWPs) in position representation

$$\langle \mathbf{x}|g_\gamma(\mathbf{q},\mathbf{p})\rangle = \left(\frac{\det(\boldsymbol{\gamma})}{\pi^N}\right)^{1/4} \exp\left\{-\frac{1}{2}(\mathbf{x}-\mathbf{q})^{\mathrm{T}}\boldsymbol{\gamma}(\mathbf{x}-\mathbf{q}) + \frac{\mathrm{i}}{\hbar}\mathbf{p}^{\mathrm{T}}\cdot(\mathbf{x}-\mathbf{q})\right\} \tag{3}$$

with a constant, real, positive definite, and diagonal width parameter matrix $\boldsymbol{\gamma}$. The integration in (2) is performed over phase space points which serve as initial conditions of classical trajectories ($\mathbf{p}_t = \mathbf{p}(\mathbf{q},\mathbf{p},t)$, $\mathbf{q}_t = \mathbf{q}(\mathbf{q},\mathbf{p},t)$). Furthermore, classical mechanics comes into play via the classical action

$$S = S(\mathbf{q},\mathbf{p},t) = \int_0^t \mathcal{L}\, \mathrm{d}t' \tag{4}$$

with the Lagrangian $\mathcal{L} = \mathcal{T} - \mathcal{V}$.

The matrix in the determinantal prefactor, which goes back to the original work of Herman and Kluk, is given in a slightly generalized form by[27,28]

$$\mathbf{h}(\mathbf{q},\mathbf{p},t) = \frac{1}{2}\left(\mathbf{m}_{11} + \boldsymbol{\gamma}\mathbf{m}_{22}\boldsymbol{\gamma}^{-1} - \mathrm{i}\hbar\boldsymbol{\gamma}\mathbf{m}_{21} + \frac{\mathrm{i}}{\hbar}\mathbf{m}_{12}\boldsymbol{\gamma}^{-1}\right) \tag{5}$$

It ensures the propagator's unitarity in the stationary phase sense[29] and consists of elements of the so-called monodromy (or stability) matrix,

$$\mathbf{M} = \begin{pmatrix} \mathbf{m}_{11} & \mathbf{m}_{12} \\ \mathbf{m}_{21} & \mathbf{m}_{22} \end{pmatrix} = \begin{pmatrix} \frac{\partial \mathbf{p}_t}{\partial \mathbf{p}} & \frac{\partial \mathbf{p}_t}{\partial \mathbf{q}} \\ \frac{\partial \mathbf{q}_t}{\partial \mathbf{p}} & \frac{\partial \mathbf{q}_t}{\partial \mathbf{q}} \end{pmatrix} \tag{6}$$

This matrix describes the time evolution of small deviations in the initial conditions and can be obtained by solving linearized Hamilton equations for the deviations.

**B. Density Matrix Formulation.** In density formalism the general solution of the Liouville–von Neumann (LvN) equation

$$\rho(\mathbf{x},\mathbf{x}';t) = \int \mathrm{d}\mathbf{x}''\, \mathrm{d}\mathbf{x}'''\, K(\mathbf{x},t;\mathbf{x}'',0)\, \rho(\mathbf{x}'',\mathbf{x}''';0) \times K^*(\mathbf{x}',t;\mathbf{x}''',0) \tag{7}$$

applies the propagator twice. Because we are interested in the dynamics of a particular DOF, the appropriate quantity to consider henceforth is the reduced density matrix, focusing only on the explicit dynamics of the system of interest (SOI).

To find the appropriate semiclassical expression, we use eq 7 together with eq 2, subdividing the position coordinate vector into a SOI and a bath part, $\mathbf{x} \equiv (\mathbf{s},\mathbf{b})$. Then the partial trace over all bath DOFs is performed, finally yielding a semiclassical expression for the corresponding reduced density matrix[25]

$$\begin{aligned}\rho_{\mathrm{S}}(\mathbf{s},\mathbf{s}';t) = \int \frac{\mathrm{d}^N p\ \mathrm{d}^N q\ \mathrm{d}^N p'\ \mathrm{d}^N q'}{(2\pi\hbar)^{2N}} \sqrt{\det[\mathbf{h}^*(\mathbf{q}',\mathbf{p}',t)\, \mathbf{h}(\mathbf{q},\mathbf{p},t)]} \\ \times\, \mathrm{e}^{\mathrm{i}(S-S')/\hbar} \langle g_{\gamma_{\mathrm{B}}}(\mathbf{q}'_{\mathrm{B},t'},\mathbf{p}'_{\mathrm{B},t})|g_{\gamma_{\mathrm{B}}}(\mathbf{q}_{\mathrm{B},t'},\mathbf{p}_{\mathrm{B},t})\rangle \\ \times\, \langle g_{\gamma_{\mathrm{S}}}(\mathbf{q}'_{\mathrm{S},t'},\mathbf{p}'_{\mathrm{S},t})|\mathbf{s}'\rangle \langle \mathbf{s}|g_{\gamma_{\mathrm{S}}}(\mathbf{q}_{\mathrm{S},t'},\mathbf{p}_{\mathrm{S},t})\rangle \\ \langle g_\gamma(\mathbf{q},\mathbf{p})|\hat{\rho}(0)|g_\gamma(\mathbf{q}',\mathbf{p}')\rangle\end{aligned} \tag{8}$$

with the initial density operator $\hat{\rho}(0)$ and the width parameter matrix divided into system and bath related submatrices $\boldsymbol{\gamma}_{\mathrm{S}}$ and


dx.doi.org/10.1021/jp305084f | J. Phys. Chem. A 2012, 116, 11199−11210

$\gamma_B$, respectively. We note that still $S$ and $S'$ is the action of the overall system. Also, the labels "S" and "B" denote the subvectors for the system and the environmental DOFs. Although the integration over phase space is usually performed by a Monte Carlo procedure,[30] the computational effort for the calculation of the $4N$-dimensional integral in eq 8 is still formidable.

**C. Thawed Gaussian Wave Packet Dynamics.** We now briefly sketch the relation of the TGWD introduced by Heller[19] to the HK approximation. To this end we note that, if the initial wave function in eq 1 is a Gaussian wave packet, a distinct advantage of the HK propagator becomes manifest.[31] Let $\Psi_\alpha(\mathbf{x},0)$ be centered around $(\mathbf{q}_\alpha, \mathbf{p}_\alpha)$. Then the integration over $\mathbf{x}'$ in eq 1 can be performed analytically and the overlap of $\Psi_\alpha(\mathbf{x},0)$ with the coherent state centered around $(\mathbf{q}, \mathbf{p})$ in eq 2 reads

$$\begin{aligned}\langle g_\gamma(\mathbf{q},\mathbf{p})|\Psi_\alpha(0)\rangle = \exp\Big\{&-\frac{1}{4}(\mathbf{q}-\mathbf{q}_\alpha)^{\mathrm{T}}\boldsymbol{\gamma}(\mathbf{q}-\mathbf{q}_\alpha)\\ &-\frac{1}{4\hbar^2}(\mathbf{p}-\mathbf{p}_\alpha)^{\mathrm{T}}\boldsymbol{\gamma}^{-1}(\mathbf{p}-\mathbf{p}_\alpha)\\ &+\frac{\mathrm{i}}{2\hbar}(\mathbf{q}-\mathbf{q}_\alpha)^{\mathrm{T}}\cdot(\mathbf{p}+\mathbf{p}_\alpha)\Big\}\end{aligned} \tag{9}$$

where, for reasons of simplicity, we assumed that both Gaussians have the same width parameter matrix $\boldsymbol{\gamma}$ to render the final expression compact. The HK propagator as applied to a Gaussian wave packet can now be approximated in a simple fashion by expanding the exponent in the resulting phase space integral around the initial wave packet center $(\mathbf{q}_\alpha, \mathbf{p}_\alpha)$ up to second order. The integration in eq 1 can then be performed analytically via Gaussian integration,[21] yielding

$$\begin{aligned}\Psi_\alpha(\mathbf{x},t) = &\left(\frac{\det(\boldsymbol{\gamma})}{\pi^N}\right)^{1/4}\det(\mathbf{m}_{22}+\mathrm{i}\hbar\mathbf{m}_{21}\boldsymbol{\gamma})^{-1/2}\times\\ &\exp\Big\{-\frac{1}{2}(\mathbf{x}-\mathbf{q}_{\alpha,t})^{\mathrm{T}}\Big(\mathbf{m}_{11}\boldsymbol{\gamma}+\frac{1}{\mathrm{i}\hbar}\mathbf{m}_{12}\Big)\times\\ &(\mathbf{m}_{22}+\mathrm{i}\hbar\mathbf{m}_{21}\boldsymbol{\gamma})^{-1}(\mathbf{x}-\mathbf{q}_{\alpha,t})\\ &+\frac{\mathrm{i}}{\hbar}\mathbf{p}_{\alpha,t}^{\mathrm{T}}\cdot(\mathbf{x}-\mathbf{q}_{\alpha,t})+\frac{\mathrm{i}}{\hbar}S(\mathbf{p}_\alpha,\mathbf{q}_\alpha,t)\Big\}\end{aligned} \tag{10}$$

We emphasize that, in contrast to the HK expression (2), this expression is given in terms of just one single trajectory with initial conditions according to the mean position of the initial Gaussian. The Gaussian form of the wave packet is retained throughout the propagation, only the position and the width change in time. In addition, it is exact for potentials being at most quadratic.[32] However, due to the additional approximation which was applied to obtain eq 10, the TGWD is obviously less accurate than the HK approximation.

**D. Semiclassical Hybrid Dynamics.** Based on the HK method and the TGWD, the SCHD for the density matrix propagation can now be presented. We start by assuming that the initial density operator can be factorized into $N$ Gaussians. This is, e.g., realized for the normal mode approximation to molecular vibrations in section V. As a generalization, which will be needed later, we consider an initial wave function in the SOI variable that is a sum of two Gaussians, $|\Psi(0)\rangle = \xi(|\Psi_1\rangle+|\Psi_2\rangle)$, with a normalization factor $\xi$ due to the finite overlap (see eqs 31 and 35). Then, the initial SOI reduced density operator is a sum $\hat{\rho}_S(0) = \xi^2\sum_{\alpha,\alpha'=1}^{2}\hat{I}_{\alpha,\alpha'}$, where each contribution

$$\hat{I}_{\alpha,\alpha'} = |\Psi_\alpha\rangle\langle\Psi_{\alpha'}| \tag{11}$$

is an outer product of two $N$-dimensional Gaussians generally located at two different phase space points labeled with the indices $\alpha$ and $\alpha'$.

Again, we start with the full density matrix in terms of HK propagators, i.e., eq 7 together with eq 2. The SCHD approximation comes into play by expanding the exponent up to second order around the center of the initial Gaussian wave packet for a subset of $N_{tg}$ DOFs and performing the corresponding phase space integral analytically. The respective DOFs are hence approximated to the level of TGWD, whereas $N_{hk} = N - N_{tg}$ DOFs are retained on the level of HK. Subsequently, we trace over all bath DOFs and finally obtain an expression for the reduced density matrix contribution (here for 1D SOI, as will be the case in section V)

$$\begin{aligned}I^S_{\alpha,\alpha'}(s,s',t) = &\int\frac{\mathrm{d}^{N_{hk}}p_{hk}\,\mathrm{d}^{N_{hk}}q_{hk}\,\mathrm{d}^{N_{hk}}p'_{hk}\,\mathrm{d}^{N_{hk}}q'_{hk}}{(2\hbar)^{2N}\pi^{2N_{hk}}\pi^{1/2}}\\ &\sqrt{\frac{\det(\boldsymbol{\gamma})\det[\mathbf{h}(\mathbf{h}')^*]}{\det(\mathbf{A})\det(\mathbf{A}'^*)\det(\boldsymbol{H})}}\\ &\times\exp\Bigg\{\begin{pmatrix}s-q_{\alpha,S,t}\\ s'-q'_{\alpha',S,t}\end{pmatrix}^{\mathrm{T}}\boldsymbol{\Lambda}\begin{pmatrix}s-q_{\alpha,S,t}\\ s'-q'_{\alpha',S,t}\end{pmatrix}\\ &+\boldsymbol{\sigma}^{\mathrm{T}}\begin{pmatrix}s-q_{\alpha,S,t}\\ s'-q'_{\alpha',S,t}\end{pmatrix}+h+\frac{i}{\hbar}(S-S')\Bigg\}\\ &\times\langle g_{\gamma_{hk}}(\mathbf{q}_{hk},\mathbf{p}_{hk})|\Psi^{(hk)}_\alpha\rangle\langle\Psi^{(hk)}_{\alpha'}|g_{\gamma_{hk}}(\mathbf{q}'_{hk},\mathbf{p}'_{hk})\rangle\end{aligned} \tag{12}$$

The expression consists of the $N_B \times N_B$ matrix

$$\mathbf{H} = -(\mathbf{K}_{BB}+\mathbf{K}'_{BB}-\boldsymbol{\gamma}_B) \tag{13}$$

and the symmetric $2\times 2$ matrix

$$\begin{aligned}\boldsymbol{\Lambda} &= \begin{pmatrix}\Lambda_{11} & \Lambda_{12}\\ \Lambda_{12}^{\mathrm{T}} & \Lambda_{22}\end{pmatrix}\\ &= \begin{pmatrix}\mathbf{K}_{SB}\mathbf{H}^{-1}\mathbf{K}_{SB}^{\mathrm{T}}+K_{SS}-\frac{\gamma_S}{2} & \mathbf{K}_{SB}\mathbf{H}^{-1}\mathbf{K}'^{\mathrm{T}}_{SB}\\ \mathbf{K}'_{SB}\mathbf{H}^{-1}\mathbf{K}_{SB}^{\mathrm{T}} & \mathbf{K}'_{SB}\mathbf{H}^{-1}\mathbf{K}'^{\mathrm{T}}_{SB}+K'_{SS}-\frac{\gamma_S}{2}\end{pmatrix}\end{aligned} \tag{14}$$

Furthermore, it contains the 2-dimensional vector

$$\boldsymbol{\sigma} = \begin{pmatrix}\sigma_1\\ \sigma_2\end{pmatrix} = \begin{pmatrix}\mathbf{K}_{SB}\mathbf{H}^{-1}\mathbf{d}-2\mathbf{K}^{\mathrm{T}}_{BS}\mathbf{q}_{\alpha,B,t}+\frac{\mathrm{i}}{\hbar}p_{\alpha,S,t}\\ \mathbf{K}'_{SB}\mathbf{H}^{-1}\mathbf{d}-2\mathbf{K}'^{\mathrm{T}}_{BS}\mathbf{q}'_{\alpha',B,t}-\frac{\mathrm{i}}{\hbar}p'_{\alpha',S,t}\end{pmatrix} \tag{15}$$

containing the vector

$$\begin{aligned}\mathbf{d} = &(\boldsymbol{\gamma}_B-2\mathbf{K}_{BB})^{\mathrm{T}}\mathbf{q}_{\alpha,B,t}+(\boldsymbol{\gamma}_B-2\mathbf{K}'_{BB})^{\mathrm{T}}\mathbf{q}'_{\alpha',B,t}\\ &+\frac{\mathrm{i}}{\hbar}(\mathbf{p}_{\alpha,B,t}-\mathbf{p}'_{\alpha',B,t})\end{aligned} \tag{16}$$


dx.doi.org/10.1021/jp305084f | J. Phys. Chem. A 2012, 116, 11199−11210

The last abbreviation is the scalar

$$h = -\left(\mathbf{q}^{\mathrm{T}}_{\alpha,\mathrm{B},t}\frac{\boldsymbol{\gamma}_{\mathrm{B}} - 2\mathbf{K}_{\mathrm{BB}}}{2} + \frac{\mathrm{i}}{\hbar}\mathbf{p}^{\mathrm{T}}_{\alpha,\mathrm{B},t}\right)\cdot\mathbf{q}_{\alpha,\mathrm{B},t} - \left(\mathbf{q}'^{\mathrm{T}}_{\alpha',\mathrm{B},t}\frac{\boldsymbol{\gamma}_{\mathrm{B}} - 2\mathbf{K}'_{\mathrm{BB}}}{2} - \frac{\mathrm{i}}{\hbar}\mathbf{p}'^{\mathrm{T}}_{\alpha',\mathrm{B},t}\right)\cdot\mathbf{q}'_{\beta,\mathrm{B},t} + \frac{1}{4}\mathbf{d}^{\mathrm{T}}\mathbf{H}^{-1}\mathbf{d} \tag{17}$$

Again "S" and "B" denote the SOI and the bath subvectors or submatrices, respectively. Further abbreviations in eq 12 are the symmetric $2N_{\mathrm{tg}} \times 2N_{\mathrm{tg}}$ matrix

$$\mathbf{A} = \begin{pmatrix} \frac{\boldsymbol{\gamma}_{\mathrm{tg}}^{-1}}{4\hbar^2} + \frac{\tilde{\mathbf{u}}\tilde{\mathbf{m}}_{21}}{2} & \frac{\mathrm{i}}{4\hbar} + \frac{\tilde{\mathbf{m}}^{\mathrm{T}}_{21}\tilde{\mathbf{v}}^{\mathrm{T}}}{2} \\ \frac{\mathrm{i}}{4\hbar} + \frac{\tilde{\mathbf{v}}\tilde{\mathbf{m}}_{21}}{2} & \frac{\boldsymbol{\gamma}_{\mathrm{tg}}}{4} + \frac{\tilde{\mathbf{v}}\tilde{\mathbf{m}}_{22}}{2} \end{pmatrix} \tag{18}$$

with the matrices

$$\tilde{\mathbf{u}} = \tilde{\mathbf{m}}^{\mathrm{T}}_{21}\boldsymbol{\gamma} + \frac{\mathrm{i}}{\hbar}\tilde{\mathbf{m}}^{\mathrm{T}}_{11}$$

$$\tilde{\mathbf{v}} = \tilde{\mathbf{m}}^{\mathrm{T}}_{22}\boldsymbol{\gamma} + \frac{\mathrm{i}}{\hbar}\tilde{\mathbf{m}}^{\mathrm{T}}_{12}, \tag{19}$$

where $\tilde{\mathbf{m}}_{ij}$ are now $N \times N_{\mathrm{tg}}$ matrices consisting of the derivatives with respect to variables carrying the label "tg" only. On the other hand, the label "hk" denotes the DOFs that are excluded from this expansion. The matrices in eqs 18 and 19 and their complex conjugate, which depend on the other half of the double phase space, also determine the symmetric matrices

$$\mathbf{K} \equiv \frac{1}{4}[\tilde{\mathbf{u}}^{\mathrm{T}} \quad \tilde{\mathbf{v}}^{\mathrm{T}}]\mathbf{A}^{-1}[\tilde{\mathbf{u}}^{\mathrm{T}} \quad \tilde{\mathbf{v}}^{\mathrm{T}}]^{\mathrm{T}}$$

$$\mathbf{K}' \equiv \frac{1}{4}[(\tilde{\mathbf{u}}'^{*})^{\mathrm{T}} \quad (\tilde{\mathbf{v}}'^{*})^{\mathrm{T}}](\mathbf{A}'^{*})^{-1}[(\tilde{\mathbf{u}}'^{*})^{\mathrm{T}} \quad (\tilde{\mathbf{v}}'^{*})^{\mathrm{T}}]^{\mathrm{T}} \tag{20}$$

whose submatrices $\mathbf{K}_{\mathrm{SS}}$, $\mathbf{K}_{\mathrm{SB}}$, and $\mathbf{K}_{\mathrm{BB}}$, which are also included in eq 12, couple the different classes of DOFs (system and bath).

We stress that in contrast to the full HK reduced density matrix expression in eq 8, the present one (eq 12) is just a $4N_{\mathrm{hk}}$-dimensional phase space integral. Also, the dynamics of the bath DOFs is still fully included in this expression. The SCHD expression in eq 12 is the method of choice for the numerical computations in section V.

## III. MODEL OF THE $I_2KR_{17}$ CLUSTER

In this work we will apply the semiclassical scheme just outlined to study the dynamics of the iodine molecule in a krypton matrix that has been investigated quite extensively in the Apkarian group.[2,4,22,33−36] Where applicable, semiclassical results will be compared with full quantum dynamics. Although the experiments are carried out in a cryogenic matrix environment, for the numerical treatment presented here we reduce the krypton environment to the first microsolvation shell. This cluster model comprises 17 Kr atoms that are arranged as a double-icosahedron surrounding the $I_2$ molecule (Figure 1). In terms of symmetry, this cluster belongs to the $D_{5h}$ point group, which is different from the experimentally realized matrix symmetry. Apart from being numerically easier to handle than a matrix model, there is also a fundamental difference of the cluster model considered here: Energy transfer from the vibrating $I_2$ molecule to the two rare gas atoms residing on the 5-fold symmetry axis can cause the latter ones to dissociate from the cluster which in principle could lead to the emergence of an observable directly related to the system-bath coupling studied here.

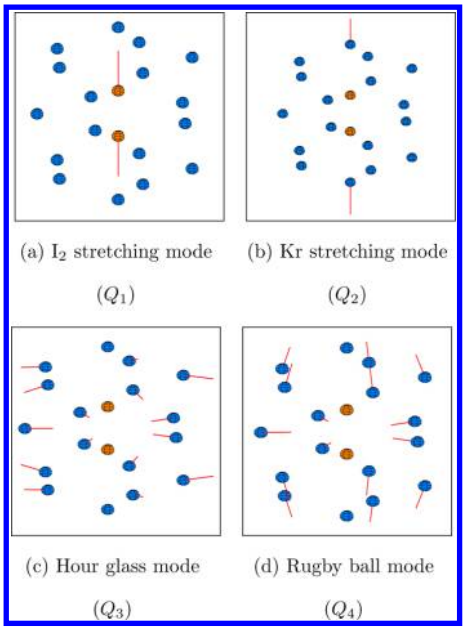


**Figure 1.** Normal modes of $I_2Kr_{17}$ with the highest symmetry, where the modes shown in (b)−(d) have the strongest coupling to the $I_2$ mode in (a). I atoms are depicted in orange; Kr atoms are blue. The red lines show the direction of atom displacements for the respective normal coordinate.

**A. Model Potentials.** In our treatment of the system, all atom−atom interactions between the iodine as well as the krypton atoms of the first solvation shell have to be accounted for. For reasons of simplicity, the full potential is approximated as a sum over all pair potentials

$$V = \sum_{J>K=1}^{N_{\mathrm{a}}} V_{KJ} \tag{21}$$

where $N_{\mathrm{a}} = 19$ is the total number of atoms and the capital letters are atom indices. Three kinds of pair potentials have to be considered, depending on the kind of atoms that interact. All potential parameters given in Table 1 are taken from ref 22, with one typographical error corrected according to ref 33. We will be considering adiabatic dynamics on a single electronic surface of $I_2$ in the following. Then the I−I interaction (each atom has a mass of $m_{\mathrm{I}} = 231323\ m_{\mathrm{e}}$) is described by the Morse potential

**Table 1. Parameters of the Model Potentials for the $I_2Kr_{17}$ Cluster**

| interaction | $D$ [$E_{\mathrm{h}}$] | $\alpha$ [$a_0^{-1}$] | $R_{\mathrm{e}}$ [$a_0$] |
|---|---|---|---|
| I−I (X state) | 0.057 | 0.99 | 5.0 |
| I−I (B state) | 0.021 | 0.98 | 5.7 |
| I−Kr (Σ) | 0.0013 | 0.79 | 7.1 |
| I−Kr (Π) | 0.00057 | 0.81 | 8.1 |
| interaction | $\sigma$ [$a_0$] | $\varepsilon$ [$E_{\mathrm{h}}$] | |
| Kr−Kr | 6.8 | 0.00063 | |


dx.doi.org/10.1021/jp305084f | J. Phys. Chem. A 2012, 116, 11199−11210

$$V_{I-I} = D_{I-I}\{1 - \exp[-\alpha_{I-I}(R_{I-I} - R_{I-I,e})]\}^2 - D_{I-I} \tag{22}$$

Below we will start with the dynamics on the electronic ground state, i.e., the X state. The corresponding period in the harmonic approximation of the potential is about 150 fs. For the dynamics after electronic excitation of the $I_2$ the Morse parameters for its electronic B state are taken. In that case, the period in the harmonic approximation is about 258 fs.

Regarding the $I_2$−Kr interaction, we use a DIM-type (diatomics in molecules[37,38]) superposition of Σ and Π potentials for the $I_2$−Kr interaction

$$V_{I_2-Kr} = \cos^2(\theta_1)V_\Sigma(R_{I(1)-Kr}) + \sin^2(\theta_1)V_\Pi(R_{I(1)-Kr}) + \cos^2(\theta_2)V_\Sigma(R_{I(2)-Kr}) + \sin^2(\theta_2)V_\Pi(R_{I(2)-Kr}) \tag{23}$$

for ground state iodine, and

$$V_{I_2-Kr} = \frac{1}{2}[V_\Sigma(R_{I(1)-Kr}) + V_\Pi(R_{I(1)-Kr})] + \frac{1}{2}[V_\Sigma(R_{I(2)-Kr}) + V_\Pi(R_{I(2)-Kr})] \tag{24}$$

for electronically excited iodine, where the index I($K$) denotes the $K$th iodine atom and $\theta_K$ is the angle between iodine molecular axis and the vector joining $K$th iodine and krypton atom. Both potentials can be modeled by the Morse potential, as well as by a Lennard-Jones potential.[5] Here, we use Morse potentials for both Σ and Π contribution.

Finally, the Kr−Kr interaction is of van der Waals type, which is here approximated by the Lennard-Jones potential

$$V_{LJ} = 4\varepsilon\frac{\sigma^6}{R_{KJ}^6}\left(\frac{\sigma^6}{R_{KJ}^6} - 1\right) \tag{25}$$

The parameter $\varepsilon$ is the well depth of the potential (similar to $D$ in the Morse oscillator) and $\sigma$ is the root of the potential. The mass of a Kr atom is $m_{Kr} = 152757\ m_e$.

**B. Normal Mode Analysis.** After geometry optimization, the $I_2Kr_{17}$ cluster emerges with $D_{5h}$ symmetry as described at the beginning of section III. The minimum energy of −0.1034 $E_h$ is close to the sum of I−I interaction, 20 I−Kr and 45 Kr−Kr nearest neighbor interactions, which is −0.09915 $E_h$. For the numerical treatment of the $I_2Kr_{17}$ cluster, we introduce normal coordinates $Q_j$ that are related to (mass-weighted) Cartesian displacement coordinates $\tilde{q}_k$ via a linear transformation

$$Q_j = \sum_k a_{kj}\tilde{q}_k \qquad \tilde{q}_k = \sqrt{m_k}\Delta x_k \tag{26}$$

with $m_k$ the mass of the atom that is associated with the $k$th DOF and where $(a)_{kj}$ is the matrix of the eigenvectors of the Hessian matrix of the potential energy function[39] from eq 21 for the electronic X state of $I_2$ (we note that, although the normal modes are determined with respect to the X state, the dynamics studied later will take place either on the X or on the B surface). More precisely, the normal modes introduced here are actually "pseudo"-normal modes, because all mixed second derivatives containing derivatives with respect to the position of an I or axial Kr atom in the Hessian matrix were neglected. This was done to obtain pure $I_2$ and $Kr_2$ symmetric stretching modes, which allows for dissociation of the two outer Kr atoms while leaving the remaining cluster intact.

In this work, we construct a reduced model comprising only four out of five totally symmetric (i.e., $A_{1g}$ representation of the $D_{5h}$ point group) normal modes of the $I_2Kr_{17}$ system. In addition to the two symmetric stretching modes of the four axial atoms, the remaining three totally symmetric modes are referred to as "hourglass", "rugby ball", and "balloon" mode. In Figure 1 these krypton normal modes as well as the $I_2$ mode are sketched. Among the Kr ("bath") modes, the axial Kr stretching is most strongly coupled to the $I_2$ (SOI) mode. The balloon mode has a considerably weaker coupling than the other totally symmetric normal modes. It will therefore be omitted in the following. Figure 2 shows 1D potential cuts along the four most important

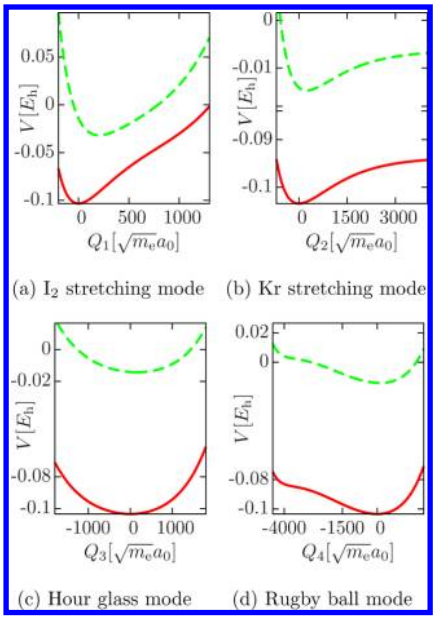


**Figure 2.** Potential cuts along single normal coordinates for $I_2$ in the electronic ground state (solid line) and $I_2$ in the electronically excited B state (dashed line).

normal modes. Because we are using ground state normal coordinates for our calculations of electronically excited iodine, potential minima of all normal coordinates are in general shifted away from zero in that case as can be seen most clearly for the $I_2$ stretch coordinate in Figure 2a. It should also be noted that the Kr stretch mode $Q_2$ is the only one that has a dissociative limit in its potential. All other normal modes $Q_i$ correspond to atom displacements such that both negative and positive values of $Q_i$ result in some atoms approaching each other. The axial iodine vibration $Q_1$, for example, has a potential cut with Morse like form; for $Q_1 > 800\ a_0\sqrt{m_e}$, however, the iodine molecule starts interacting with the axial Kr atoms which prevents it from dissociating.

With this model at hand, we have reduced the complexity of the 19-atomic system with 51 internal (vibrational) DOFs in a way that (quantum) dynamical calculations are feasible, where the complexity can be gradually enhanced by adding more and more normal modes, thereby creating a hierarchy of models. In passing we note that some of the normal modes considered here closely resemble those obtained for dihalogens in a rare gas matrix.[38]

## IV. NUMERICAL RESULTS FOR GROUND STATE DYNAMICS

With the atomic interactions defined, we are now in a position to perform dynamical simulations for the system of interest.


dx.doi.org/10.1021/jp305084f | J. Phys. Chem. A 2012, 116, 11199−11210

To justify our hierarchical model, we will first compare our numerical rates for the loss of vibrational coherence on the electronic ground state of $I_2$ with the temperature dependent experimental ones,[4] as has been done previously using mixed quantum-classical approaches.[5,6] All full quantum results in this and the next section have been obtained with the split-operator method (SPO)[40] as implemented in the WavePacket software.[41]

**A. Quantities of Interest and Initial States.** We use two different measures for decoherence. On the one hand, the *purity*

$$P(t) = \mathrm{tr}(\hat{\rho}_S^{\,2}(t)) \tag{27}$$

describes the degree of pure state content of a system, taking values between 1 and $1/n$, where $n$ is the number of states taking part in the dynamics.[42] On the other hand, the *coherence* $\Pi_{kj}(t)$ between two vibrational eigenstates $|k\rangle$ and $|j\rangle$ of a system is defined as[5,6]

$$\Pi_{kj}(t) = |\rho_{kj}(t)| \tag{28}$$

where $\rho_{kj}(t)$ is the matrix element $\rho_{kj}(t) = \langle k|\hat{\rho}_S(t)|j\rangle$. Our initial state is assumed to be a product state

$$|\Psi\rangle = |\Psi_S\rangle|\Psi_B\rangle \tag{29}$$

of system $|\Psi_S\rangle$ and bath part $|\Psi_B\rangle$ with

$$|\Psi_B\rangle = \prod_{n=1}^{N} |\psi_{B,n}\rangle \tag{30}$$

where the number of bath modes $N$ is at most 3 for the quantum mechanical calculations. In the system DOF ($I_2$ stretching mode), the initial state is a superposition state, consisting of either two Gaussians or two numerically calculated vibrational eigenstates of $I_2$ in the rigid Kr cage. The coherence of two initial vibrational eigenstates is investigated to achieve results that can be compared with the experimental ones[4] as well as with results from earlier theoretical works.[5,6] As in the previous works, the initial superposition comprises the vibrational ground state $|0\rangle$ and a vibrationally excited eigenstate $|n\rangle$.

The purity of two initial GWPs is considered in particular to be used in the next section for the SCHD. For that method, GWPs are an ideal initial state due to their straightforward sampling, and the purity, depending on the reduced density matrix only, is an easily accessible quantity of interest. For that case, the initial Schrödinger catlike state of the system is

$$\begin{aligned}|\Psi_S\rangle &\equiv |\Psi_{cat}\rangle \\ &= \frac{1}{\sqrt{2}}\{1 + e^{-(P_{1,\alpha}-P_{1,\alpha'})^2/4\gamma}\cos[Q_1(P_{1,\alpha} - P_{1,\alpha'})]\}^{-1/2} \\ &\quad (|\Psi_\alpha\rangle + |\Psi_{\alpha'}\rangle)\end{aligned} \tag{31}$$

Both Gaussians are centered at $Q_1 = 0$, i.e., at the potential minimum. The initial momenta are chosen to be $P_{1,\alpha} = 0$ and $P_{1,\alpha'} \neq 0$ such that one Gaussian is in the vibrational ground state and the energy of the other one corresponds to the energy of the $n$th excited eigenstate. The width parameter of both Gaussians corresponds to the width of the ground state of the harmonic approximation or equivalently to the eigenfrequency of the $I_2$ stretching mode: $\gamma_1 = 22.29\ a_0^{-2}$.

To observe decoherence effects without zero-point energy modifications,[43] we have to treat finite temperature baths. This requirement determines the initial states of all bath DOFs. For the full quantum case, a finite temperature bath can be simulated by a thermal average over a sufficiently large number of independent wave packet calculations according to

$$i\frac{\partial}{\partial t}\hat{\rho}(t) = \sum_n e^{-\beta\hat{H}_B}[\hat{H},\hat{\rho}_n(t)] \tag{32}$$

where $\hat{H}$ and $\hat{H}_B$ are total and bath Hamiltonian, respectively. Equation 32 is a solution of the LvN equation only for vanishing system-bath coupling $\hat{H}_{SB} = \hat{0}$, which we assume to be approximately fulfilled. Also, we assume the potentials of the bath modes close to $Q_{B,i} = 0$ ($i$ = 2, ..., 4) to be sufficiently harmonic that the initial bath states can be chosen as eigenstates of harmonic oscillators with frequencies corresponding to the eigenvalues found in the normal-mode analysis.

**B. Coherence for Different Numbers of Bath Modes.** First, we consider an initial superposition of ground and excited vibrational eigenstate in the system DOF

$$|\Psi_S(0)\rangle = \frac{1}{\sqrt{2}}(|0\rangle + |n\rangle) \tag{33}$$

with corresponding initial reduced density matrix

$$\hat{\rho}_S(0) = \frac{1}{2}(|0\rangle\langle 0| + |0\rangle\langle n| + |n\rangle\langle 0| + |n\rangle\langle n|) \tag{34}$$

making the initial coherence $\Pi_{0n}(0) = |\langle 0|\hat{\rho}_S(0)|n\rangle| = 0.5$. For a start, we choose $T$ = 45 K and $n$ = 20 to get a significant loss of coherence on a short time scale.

Our cluster approach allows for a hierarchy of models, adding one bath DOF at a time. The first bath mode to be added is the vibration of the two axial Kr atoms along the iodine molecular axis, described by normal coordinate $Q_2$. It has the strongest coupling to the system in the sense that the decay of vibrational coherence is faster than in any other 2D calculation. As can be seen from the results of full quantum calculations displayed in Figure 3a, $\Pi_{0n}(t)$ shows oscillatory behavior as well as

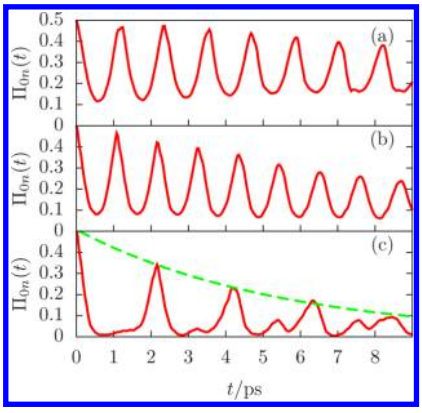


**Figure 3.** Coherence decay of $I_2$ vibration for different number of bath DOFs at $T$ = 45 K (full quantum results). (a) One bath mode: axial Kr. (b) Two bath modes: axial Kr and hourglass. (c) Three bath modes: axial Kr, hourglass and rugby ball. The dashed line shows the exponential fit for the decay of $\Pi_{0n}(t)$.

exponential decay. The oscillation period of about 1170 fs is close to the harmonic approximation of the bath DOF (1102 fs).

Increasing the complexity of the problem by adding the hourglass normal mode $Q_3$ and thus allowing for movement of the Kr ring atoms according to Figure 1c yields a slightly shorter oscillation period and faster decay of vibrational coherence (Figure 3b). If the fourth normal mode $Q_4$ (rugby ball mode,


dx.doi.org/10.1021/jp305084f | J. Phys. Chem. A 2012, 116, 11199−11210

Figure 1d) is taken into account, the decay is very much enhanced and the oscillation period doubles, as shown in Figure 3c. This strong change might be due to the fact that axial Kr stretch with 1102 fs and hourglass with 1144 fs have similar oscillation periods, whereas rugby ball mode with 1513 fs is clearly off-resonant. As expected, the number of bath modes is crucial for the decoherence dynamics of the system. In the following, we will show results from 4D full quantum calculations only. In terms of numerical effort, it takes 128 grid points for the system DOF and either 16 or 32 grid points for each bath DOF to perform these calculations. The time step for the SPO is 1 fs.

**C. Comparison with Experimental Results.** Figure 4 shows the coherence from calculations starting from a

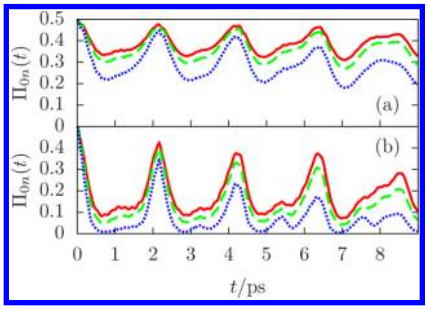


**Figure 4.** Vibrational coherence of $I_2$ in a Kr microsolvation environment for $T$ = 10 K (solid), $T$ = 20 K (dashed), and $T$ = 45 K (dotted) from 4D full quantum calculations: (a) $n$ = 10; (b) $n$ = 20.

superposition of vibrational ground and excited state with $n$ = 10 and $n$ = 20, respectively. The qualitative behavior is the same as in the experiment. Higher bath temperatures result in faster loss of coherence. It also becomes clear that the energy of the excited eigenstates has a strong influence on the dynamics: a superposition with a high-lying excited eigenstate undergoes fast decoherence. Fitting the peaks in the graphs from Figure 4 with the experimentally expected quantitative behavior $\Pi_{0n}(t) \sim e^{-\Gamma_{0n}t}$ as shown in Figure 3c, rates $\Gamma_{0n}$ for the loss of vibrational coherence can be extracted and compared with the fits to experimental data (Table 2). In spite of our model comprising

**Table 2. Comparison of Decoherence Rates $\Gamma_{0n}$ from Fits to Experiments[4] with Our 4D Full Quantum Calculations**

| | 45 K | | 20 K | | 10 K | | |
|---|---|---|---|---|---|---|---|
| | $n$ = 10 | $n$ = 20 | $n$ = 10 | $n$ = 20 | $n$ = 10 | $n$ = 15 | $n$ = 20 |
| $\Gamma_{0n,\mathrm{exp}}$ ($ps^{-1}$) | 0.100 | 0.34 | 0.040 | 0.10 | 0.029 | 0.044 | 0.060 |
| $\Gamma_{0n,\mathrm{sim}}$ ($ps^{-1}$) | 0.053 | 0.18 | 0.025 | 0.09 | 0.015 | 0.032 | 0.059 |

only the first solvation shell and using only four normal modes, our decoherence rates differ from the experimental results at most by a factor of 2. For all computations listed in Table 2, the rates are smaller than the experimental ones, which is due to two reasons. First, we use only three bath modes. As shown in Figure 3, the loss of coherence is enhanced if the number of bath modes is increased. Therefore, one might expect the rates to get bigger if more bath modes are included. Second, we get a 2-fold error by the way we simulate finite bath temperature. For high temperature, in this case 45 K, the number of bath states with a significant weight $e^{-\beta E_{B,n}}$ gets too big to consider all contributions. At the same time, higher-lying bath states have to be taken into account; for those states the assumption of a harmonic potential is no longer valid. For $n$ = 20, the influence of the temperature can be seen very clearly. At $T$ = 10 K, the rate agrees almost exactly with the experimental one. Here, the summed weight of the $m$ contributing bath states as a fraction of the total partition function, $\sum_{j=1}^{m} e^{-\beta E_{B,j}} / \sum_{j=1}^{\infty} e^{-\beta E_{B,j}}$, is almost 1. At $T$ = 45 K, this fraction is only 0.85 (with $m$ = 30). Consequently, the rate is considerably smaller than the experimental one.

We stress that by using only four out of 51 normal modes, a very good agreement with experimental results, and therefore also with purely classical simulations taking explicitly into account 108 atoms,[5,6] can be achieved.

**D. Purity vs Vibrational Coherence and GWP vs Vibrational Eigenstate.** After having established good qualitative and quantitative agreement of our model with experimental results, we will now introduce the purity as a viable alternative measure for coherence of our system, and we also show that simulations with initial superpositions of GWPs display similar dynamics as simulations with eigenstates as initial states. In Figure 5, vibrational coherence (multiplied by 2 to get

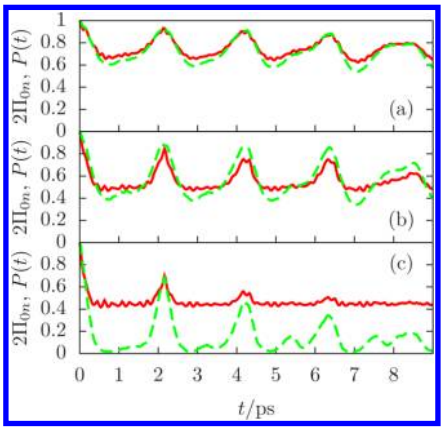


**Figure 5.** Purity $P(t)$ (solid) and vibrational coherence $2\Pi_{0n}(t)$ (dashed) of $I_2$ DOF for (a) $n$ = 10, $T$ = 20 K, (b) $n$ = 15, $T$ = 10 K, and (c) $n$ = 20, $T$ = 45 K from full quantum calculations.

values between 0 and 1) and purity are shown for three different setups. The qualitative evolutions are identical, with both quantities undergoing exponential decay. However, decay rates are not the same. The same holds for the limit for $t \to \infty$ of both quantities, as illustrated especially in Figure 5c. Due to both quantities displaying the same qualitative behavior, it can be concluded that the loss of vibrational coherence corresponds to a loss of quantum character of the system DOF in general. Therefore, we will use the purity as the computationally easier measure for decoherence henceforth.

The influence of the form of the initial wave packet can be seen in Figure 6, in which either Schrödinger catlike states, i.e., superpositions of two GWPs according to eq 31, or superpositions of two eigenstates as before are used as initial states. In the case of GWPs, one Gaussian is chosen to be identical to the ground vibrational eigenstate, and the other one is placed in the potential minimum and has nonzero momentum such that it has the same energy as a given excited eigenstate. In effect, we only change the shape of the excited state. Differences in the details of the purity are visible for all three examples; however, the overall time evolution is the same. Especially the peaks indicating purity revivals appear at the same points in time and have identical


dx.doi.org/10.1021/jp305084f | J. Phys. Chem. A 2012, 116, 11199−11210

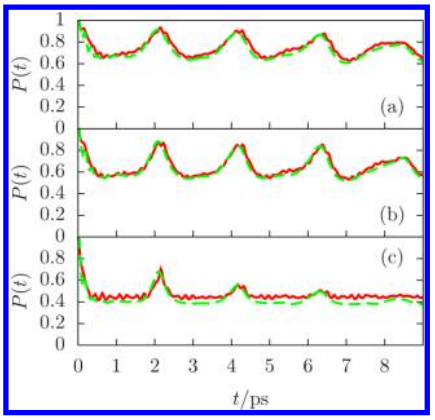


**Figure 6.** Purity $P(t)$ of $I_2$ DOF for (a) $n = 10$, $T = 20$ K, (b) $n = 15$, $T = 10$ K, and (c) $n = 20$, $T = 45$ K from full quantum calculations. Initial states are either eigenstates (solid line) or Gaussians with energy corresponding to the respective eigenstate (dashed line).

heights, pointing to similar bath dynamics. The smaller oscillations on top of the eigenstate purity are due to the more sophisticated form of the highly excited eigenstate when compared with a simple GWP. The loss of quantum characteristics is mainly dominated by the initial energy rather than by its detailed form.

## V. NUMERICAL RESULTS FOR EXCITED STATE DYNAMICS

In intriguing experiments on excited state dynamics of the Apkarian group[2] the generation of vibrational Schrödinger cat-like states in the Kr bath has been postulated. In the remainder of this paper we therefore concentrate on describing the dynamics of an initial cat state of the $I_2$ evolving on the electronic B surface. Now we are interested in the qualitative behavior only and therefore restrict ourselves to the case $T = 0$. For this purpose, we choose an arbitrary superposition of two Gaussians

$$|\Psi_{cat}\rangle = \frac{1}{\sqrt{2}}(1 + e^{-(\gamma_s/4)(Q_{1,\alpha}-Q_{1,\alpha'})^2})^{-1/2}(|\Psi_\alpha\rangle + |\Psi_{\alpha'}\rangle) \quad (35)$$

where one Gaussian is centered at the minimum of the B state at $Q_{1,a} = 204.1\ a_0(m_e)^{1/2}$ and the other Gaussian at the repulsive side of the potential at $Q_{1,b} = 22.63\ a_0(m_e)^{1/2}$. Both Gaussians start at zero initial momentum, thus having energies that correspond to energies of vibrational ground and 20th excited state, respectively, of $I_2$ in the electronically excited B state. The width parameters of both Gaussians are the same as for the ground state dynamics. In the bath DOFs a single GWP is initially located at $Q_i = 0$ $(i = 2, ..., 4)$. However, due to $I_2$ being electronically excited now, this no longer corresponds to the potential minimum. All bath DOFs have zero initial momentum and their width parameters correspond to the eigenfrequency of the respective normal mode, i.e., $\gamma_2 = 60.21\ a_0^{-2}$, $\gamma_3 = 61.36\ a_0^{-2}$, and $\gamma_4 = 70.56\ a_0^{-2}$.

The main difference to the ground state dynamics described in the previous section is that the electronically excited iodine molecule induces a partial dissociation of the axial Kr molecules, i.e., the Kr stretching mode $Q_2$. This dissociation leads to a suppression of the purity revivals, as can be seen from a comparison of Figures 7a and 11a with Figure 6. Numerically, it requires a higher number of grid points and the use of absorbing boundary conditions to treat this dissociating bath mode with full quantum mechanics. Due to hourglass mode $Q_3$ and rugby ball mode $Q_4$ also not starting at the potential energy minimum, these bath modes require a higher number of grid points, as well. In the examples below, 128, 512, 64, and 128 grid points have been used for $Q_1$, $Q_2$, $Q_3$, and $Q_4$, respectively. For both SCHD and SPO, the time step was 1 fs.

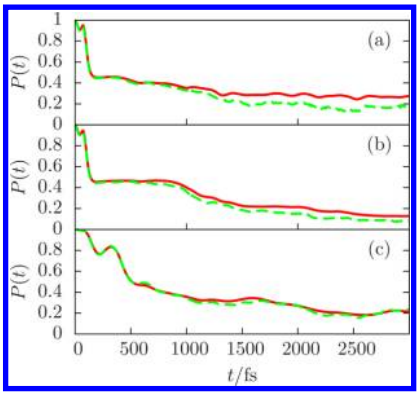


**Figure 7.** Time evolution of the purity of various normal modes for $I_2Kr_{17}$ with $I_2$, $Kr_2$, and hourglass mode: (a) $I_2$ stretching mode $Q_1$; (b) $Kr_2$ stretching mode $Q_2$; (c) hourglass mode $Q_3$. Solid lines: quantum results. Dashed lines: SCHD results.

**A. Three Normal Modes: Comparison of SCHD with Full Quantum Results.** In this section, we compare three-dimensional SCHD results with full quantum ones. First, the $I_2$, $Kr_2$, and hourglass modes are considered, for which the purities are shown in Figure 7 on a time scale in the order of 12 vibrational periods of $I_2$ in the B state. Within the SCHD treatment, the $I_2$ mode $Q_1$ is treated on the level of the HK approximation as well as the $Kr_2$ stretching mode $Q_2$, because its coupling to the $I_2$ mode is the strongest compared with all other normal modes. In contrast, we exploit the relatively weak coupling of the hourglass mode $Q_3$ by treating this DOF on the level of TGWD. We find that the agreement between the purities is very good, even for the hourglass mode, which is treated with a cruder approximation than the other modes. The largest deviation becomes manifest in the $I_2$ mode at larger times, where the SCHD result is below the full quantum one. However, up to this deviation, the quantum results are well reproduced by SCHD. We note that for this system the deviation of the norm from unity is maximally 10% at larger times in the SCHD.

Next, the hourglass mode $Q_3$ is replaced by the rugby ball mode $Q_4$. The corresponding purities are plotted in Figure 8.

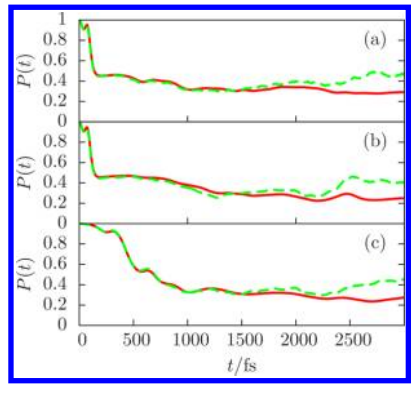


**Figure 8.** Time evolution of the purity of various normal modes for $I_2Kr_{17}$ with $I_2$, $Kr_2$, and rugby ball mode: (a) $I_2$ stretching mode; (b) $Kr_2$ stretching mode; (c) rugby ball mode. Solid lines: quantum results. Dashed lines: SCHD results.


dx.doi.org/10.1021/jp305084f | J. Phys. Chem. A 2012, 116, 11199−11210

Here the agreement of the SCHD with quantum results in all three modes is even better than in the previous case, except for times above $t$ = 2300 fs, where the SCHD result for all modes is above the quantum one. Also, the norm deviates from unity by less than 15% at larger times. We note in passing that for all SCHD results the necessary number of sampled trajectories is $10^5$, which is reasonable considering the eight-dimensional phase space integral and the length of the time scale.

The excellent agreement of the purities in the hourglass and rugby ball mode is surprising, the more so as both modes are treated on the level of an approximation in which the corresponding (reduced) density was assumed to retain its Gaussian form. On the other hand, one might assume that in the full quantum treatment the initial Gaussian shape of the reduced density is distorted after a few periods due to the anharmonicity of the potential energy surfaces. To shed light on this seemingly contradictory issue, we investigate the time evolution of the reduced density in the hourglass and rugby ball mode in more detail.

To this end, a snapshot of the SCHD Wigner function[44]

$$W(s,\tilde{p}_S) = \frac{1}{\pi\hbar}\int \mathrm{d}\zeta\ \hat{\rho}_S(s-\zeta,s+\zeta;t)\mathrm{e}^{2\mathrm{i}\tilde{p}_s\zeta/\hbar} \tag{36}$$

is plotted in Figure 9 for the hourglass mode at $t$ = 1320 fs, which is after about five $I_2$ periods. A direct SCHD expression for

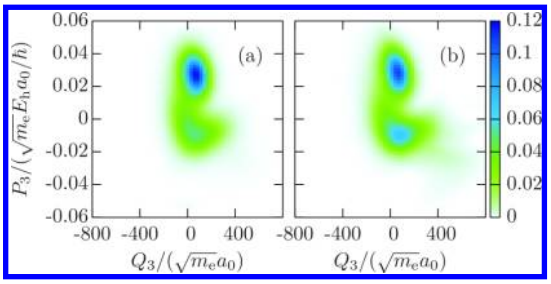


**Figure 9.** Snapshot of the hourglass mode Wigner function at 1320 fs considering three normal modes from full quantum simulation (a) and from SCHD (b).

$W(s,\tilde{p}_s)$ is derived in Appendix A; this SCHD result is compared with the full quantum one. The agreement of both results is obvious. Furthermore, we find that the initial superposition of two locally separated wave packets in the $I_2$ is reflected in the hourglass mode due to their mutual coupling. As one can see from Figure 9, both parts of the Wigner function are of slightly distorted Gaussian form, even in the SCHD. This circumstance suggests that the TGWD DOFs generally do not keep their Gaussian shape in the SCHD. To see this more clearly, the Wigner function for the rugby ball mode is shown in Figure 10 at

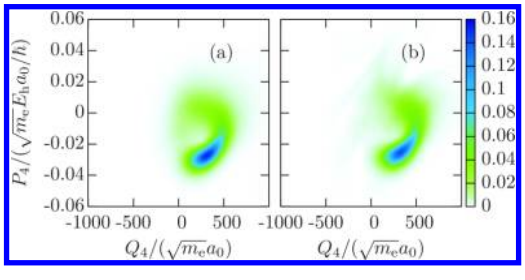


**Figure 10.** Snapshot of the rugby ball mode Wigner function at 1800 fs considering three normal modes from full quantum simulation (a) and from SCHD (b).

time $t$ = 1800 fs. The quantum result is very well reproduced by the SCHD and apparently its shape is different from the shape of a minimum uncertainty wave packet or a superposition of two of them.

To elucidate this phenomenon, we recall that the DOFs on both levels of approximation, HK and TGWD, are coupled via classical dynamics. While the initial HK phase space points are sampled within the numerical integration, the initial phase space point of a TGWD DOF is fixed at the center of the corresponding initial GWP. However, due to the coupling to the HK DOFs, the trajectories associated with a TGWD DOF vary due to the coupling to the different initial conditions (leading to different histories).[45] Therefore, strictly speaking, the integration over the HK DOFs comes along with an integration over a set of "thawed Gaussian"-trajectories in the SCHD, and thus the reduced density of a TGWD DOF is *not* restricted to a Gaussian shape. This confirms our assumption that an approximation on the level of TGWD applied to a DOF which is coupled to other HK DOFs, as in the SCHD, can still be accurate, even if weakly affected by anharmonic dynamics.

**B. Four Normal Modes.** So far, we have compared three-dimensional SCHD results with full quantum ones and found good agreement. Now we increase the number of DOFs by considering all four of the most important normal modes, i.e., $I_2$, $Kr_2$, hourglass, and rugby ball. For iodine in the electronic B state, a 4D full quantum treatment with the SPO would be numerically overly expensive, because due to the aforementioned dissociation of the axial Kr atoms, the necessary grid size for a wave function with more than 3 DOFs increases beyond the memory capacity of a standard desktop computer, even if absorbing boundary conditions are applied. In contrast, for the SCHD this is no restriction and thus it can be applied. Again, the phase space sampling within the framework of the numerical integration is performed only for the $I_2$ and $Kr_2$ modes, whereas the rugby ball and hourglass modes are still treated on the level of TGWD. We note in passing that also in the four-dimensional calculation $10^5$ sampling points were used for the Monte Carlo integration.

In Figure 11, the purities obtained with SCHD for each of the considered modes are plotted and compared for the three- and

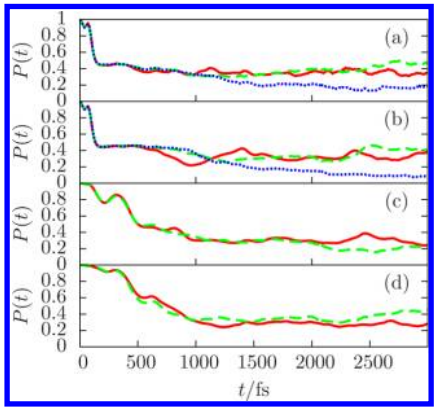


**Figure 11.** Time evolution of the SCHD purity of various normal modes. (a) $I_2$ mode with $Kr_2$, hourglass, and rugby ball mode (solid line), $Kr_2$ and rugby ball mode (dashed line), and $Kr_2$ and hourglass mode (dotted line). (b) $Kr_2$ mode with $I_2$, hourglass, and rugby ball mode (solid line), $I_2$ and rugby ball mode (dashed line), and $Kr_2$ and hourglass mode (dotted line). (c) Hourglass mode with $I_2$, $Kr_2$, and rugby ball mode (solid line) and $I_2$ and $Kr_2$ mode (dashed line). (d) Rugby ball mode with $I_2$, $Kr_2$, and hourglass mode (solid line) and $I_2$ and $Kr_2$ mode (dashed line).


dx.doi.org/10.1021/jp305084f | J. Phys. Chem. A 2012, 116, 11199−11210

four-dimensional case. A comparison of the different purities for every normal mode reveals only small differences between results for the four- and three-dimensional case. Particularly, the purities of the cage modes show only slight deviations between the results obtained for different numbers of DOFs. Hence, for the chosen initial state in the $I_2$, we could assume that for a certain cage mode it is almost insignificant, whether or not the other cage mode is considered in the propagation.

Of course, the purity does not give all information about a state. It only reveals information about the "mixedness" of a state. Therefore, to see the influence of an additional normal mode on a subsystem, the Wigner functions of the rugby ball mode are shown in Figure 12 for both the three- and four-dimensional case.

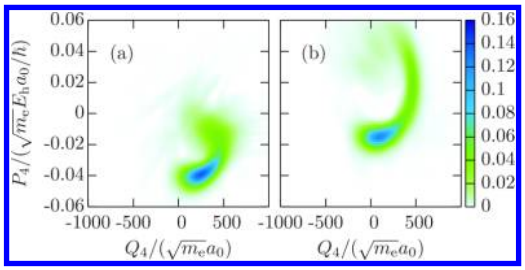


**Figure 12.** Snapshot of the rugby ball mode SCHD Wigner function at 1860 fs from calculation with three normal modes (a) and four normal modes (b).

The comparison of both snapshots, taken at the same time $t$ = 1860 fs, shows clear differences, especially in the momentum width and also in the position of the maxima. Consequently, we conclude that indeed it is relevant for the dynamics of a cage mode, whether or not another cage mode is considered in the dynamics of the overall system.

**C. Comparison with Experimental Results.** At last, we shortly compare our results with experimental findings from the Apkarian group, who inferred from their four-wave mixing experiments that a coherent superposition between different vibrational states of the bath is created.[2] As can be seen in Figure 9, the initial conditions used for our calculations generate a vibrational superposition in the hourglass bath mode $Q_3$. However, the superposition is incoherent, which is indicated by the lack of an interference pattern with negative parts between both "packets" in the Wigner function (Heller's "dangerous cross terms"[46]). The lack of interference in the bath modes might just be due to the dissociation-induced lack of purity revivals. That is why we have performed calculations for a variety of initial conditions and sets of bath modes to find an initial setup for electronically excited iodine that results in purity revivals as well as coherent superpositions of bath states. Apart from "artificial" initial cat states with arbitrarily chosen positions and momenta according to eq 35 and 31, we also used initial conditions closer to the experiment. For that, we ran 1D full quantum calculations on two coupled electronic surfaces, starting with the cluster at its equilibrium position in the electronic X state and irradiating with two laser pulses with frequencies, delay time, and pulse durations according to ref 2, to provide a superposition of two GWPs in $Q_1$ as initial condition for our subsequent 2D or 3D calculations on the B state. Some minor oscillations in the system purity have been observed, but the energetic distance between the initial GWPs turned out to be too small to split up the bath Gaussians.

With certain "artificial" initial conditions, such purity revivals can be observed, as well. One example is shown in Figure 13, where the wave function was a cat state according to eq 35 with

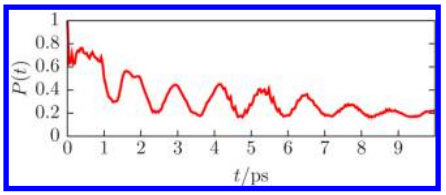


**Figure 13.** Purity of iodine mode from 3D full quantum calculation with Kr stretching and hourglass mode. As seen in the experiment, the purity shows revivals while decaying exponentially.

initial Gaussians centered at 78 $(m_e)^{1/2}a_0$ and 378 $(m_e)^{1/2}a_0$, respectively, corresponding to both Gaussian having the energy of the seventh eigenstate. On the other hand, all calculations with artificial initial states have shown that every time a bath mode splits up into two Gaussians, this superposition is incoherent and the purity of the respective bath mode is at a local minimum, no matter if there are purity revivals in the system or not.

## VI. SUMMARY AND OUTLOOK

We have studied the ground as well as excited electronic state dynamics of wave packets for the $I_2Kr_{17}$ cluster. A pseudo normal mode analysis has been undertaken to make the dynamics amenable for quantum calculations. As a first central result of this paper, we could show that good agreement with experimental (and previous classical) results can be achieved already with four DOFs, particularly for high initial excitation and low temperature.

Second, in the case of excited state dynamics and for zero temperature, we employed a semiclassical hybrid scheme as quantum calculations become increasingly cumbersome so that four normal modes are beyond the capabilities of standard present-day computers. After finding good agreement between semiclassical and full quantum results for three normal modes, we proceeded to investigate the dynamics of four normal modes in SCHD. Although the hybrid scheme employs thawed Gaussians for the bath DOFs, we could show that non-Gaussian distortions are manifested in our results.

As in the experiment, partial purity revivals have been observed for certain initial conditions. Other than inferred from the experiment, which was performed at finite temperature, we did not see any signatures of cat states in the bath, even for $T$ = 0. Only incoherent superpositions of different vibrational bath states were generated. In future investigations we intend to investigate different cluster or matrix geometries to study the influence of symmetry and size of the Kr environment on the decoherence dynamics. Another direction is to apply finite-temperature SCHD[26] to improve quantitative agreement with experimental data also for other regions of temperature/excitation parameter space. Finally, the influence of further normal modes on the decoherence dynamics will be the objective of future studies, where we intend to include more than four normal modes in SCHD calculations to corroborate the convergence of our reduced dimensionality results toward the bulk results.

## APPENDIX A: SCHD EXPRESSION OF THE WIGNER FUNCTION

We consider a one-dimensional SOI. In density matrix formalism the Wigner function has already been defined in eq 36 as

$$W(s,\tilde{p}_S) = \frac{1}{\pi\hbar}\int d\zeta\ \langle s-\zeta|\hat{\rho}|s+\zeta\rangle e^{2i\tilde{p}_S\zeta/\hbar} \tag{A1}$$


dx.doi.org/10.1021/jp305084f | J. Phys. Chem. A 2012, 116, 11199−11210

For reasons of clarity, the momentum of the Wigner representation $\tilde{p}_S$ is introduced to distinguish it from the system momentum $p_S$, which is part of the phase space integration variables in the SCHD. Inserting the SCHD expression of the reduced density from eq 12, the $\zeta$-dependent terms in the exponent of eq A1 then give

$$e = -(-\Lambda_{11} + 2\Lambda_{12} - \Lambda_{22})\zeta^2 + \left[-2(s - q_{\alpha,S,t})\Lambda_{11} + 2(q_{\alpha,S,t} - q_\alpha)\Lambda_{12} + 2(s - q_{\alpha,S,t})\Lambda_{22} - \sigma_1 + \sigma_2 + \frac{2i}{\hbar}\tilde{p}_S\right]\zeta + (s - q_{\alpha,S,t})^2\Lambda_{11} + (s - q'_{\alpha,S,t})^2\Lambda_{22} + 2(s - q_{\alpha,S,t})(s - q'_{\alpha,S,t})\Lambda_{12} + (s - q_{\alpha,S,t})\sigma_1 + (s - q'_{\alpha,S,t})\sigma_2 \quad (A2)$$

This is now an exponent of quadratic form in $\zeta$, for which the integral in eq A1 can be calculated analytically by applying a Gaussian integration formula. The Wigner function then becomes

$$W(s,\tilde{p}_S) = \int \frac{d^{N_{hk}}p_{hk}\, d^{N_{hk}}q_{hk}\, d^{N_{hk}}p'_{hk}\, d^{N_{hk}}q'_{hk}}{(2\hbar)^{2N}\pi^{2N_{hk}}\pi\hbar} \sqrt{\frac{\det(\boldsymbol{\gamma})\, R(R')^*}{\det(\mathbf{A})\, \det(\mathbf{H})}} \sqrt{\frac{1}{(-\Lambda_{11} + 2\Lambda_{12} - \Lambda_{22})}} \exp\left\{\tilde{e} + h + \frac{i}{\hbar}(S - S')\right\} \langle g_{\gamma_S}(q_S,p_S)|\Psi_\alpha\rangle\langle\Psi_\alpha|g_{\gamma_S}(q'_S,p'_S)\rangle \quad (A3)$$

where the expression

$$\tilde{e} = \begin{pmatrix} s - q_{\alpha,S,t} \\ s - q'_{\alpha,S,t} \end{pmatrix}^T \mathcal{Y} \begin{pmatrix} s - q_{\alpha,S,t} \\ s - q'_{\alpha,S,t} \end{pmatrix} + \boldsymbol{\chi}^T \begin{pmatrix} s - q_{\alpha,S,t} \\ s - q'_{\alpha,S,t} \end{pmatrix} - \frac{1}{\hbar^2(-\Lambda_{11} + 2\Lambda_{12} - \Lambda_{22})}\tilde{p}_S^2 + \frac{2i\left[(q'_{\alpha,S,t} - q_{\alpha,S,t})\Lambda_{12} - \frac{\sigma_1}{2} + \frac{\sigma_2}{2}\right]}{\hbar(-\Lambda_{11} + 2\Lambda_{12} - \Lambda_{22})}\tilde{p}_S + \frac{\left[(q'_{\alpha,S,t} - q_{\alpha,S,t})\Lambda_{12} - \frac{\sigma_1}{2} + \frac{\sigma_2}{2}\right]^2}{-\Lambda_{11} + 2\Lambda_{12} - \Lambda_{22}} \quad (A4)$$

results from the integration over $\zeta$. It consists of the matrix

$$\mathcal{Y} = \begin{pmatrix} \frac{\Lambda_{11}^2}{2\Lambda_{12} - \Lambda_{11} - \Lambda_{22}} + \Lambda_{11} & \frac{\Lambda_{11}\Lambda_{22}}{2\Lambda_{12} - \Lambda_{11} - \Lambda_{22}} - \Lambda_{12} \\ \frac{\Lambda_{11}\Lambda_{22}}{2\Lambda_{12} - \Lambda_{11} - \Lambda_{22}} - \Lambda_{12} & \frac{\Lambda_{22}^2}{2\Lambda_{12} - \Lambda_{11} - \Lambda_{22}} + \Lambda_{22} \end{pmatrix} \quad (A5)$$

and the vector

$$\boldsymbol{\chi} = \begin{pmatrix} -\frac{\frac{2i}{\hbar}\tilde{p}_S\Lambda_{11} + 2\left[(q'_{\alpha,S,t} - q_{\alpha,S,t})\Lambda_{12} - \frac{\sigma_1}{2} + \frac{\sigma_2}{2}\right]\Lambda_{11}}{-\Lambda_{11} + 2\Lambda_{12} - \Lambda_{22}} + \sigma_1 \\ \frac{\frac{2i}{\hbar}\tilde{p}_S\Lambda_{22} + 2\left[(q'_{\alpha,S,t} - q_{\alpha,S,t})\Lambda_{12} - \frac{\sigma_1}{2} + \frac{\sigma_2}{2}\right]\Lambda_{22}}{-\Lambda_{11} + 2\Lambda_{12} - \Lambda_{22}} + \sigma_2 \end{pmatrix} \quad (A6)$$

Thus as in the semiclassical hybrid reduced density, only the numerical calculation of the phase space integral is left to obtain the SCHD Wigner function.

## AUTHOR INFORMATION


### Corresponding Author

*E-mail: max.buchholz@mailbox.tu-dresden.de.


### Notes

The authors declare no competing financial interest.

## ACKNOWLEDGMENTS

We gratefully acknowledge financial support by the Deutsche Forschungsgemeinschaft (GR 1210/4-1,2), and allocation of computational resources by the Zentrum für Informationsdienste und Hochleistungsrechnen (ZIH) of the Technische Universität Dresden. P.J. thanks the Czech Science Foundation for support via grant P208/12/G016 and the Academy of Sciences for the Praemium Academie Award. For help with the construction of the normal modes we thank Martin Mucha.

## REFERENCES


(1) Bihary, Z.; Karavitis, M.; Apkarian, V. A. *J. Chem. Phys.* **2004**, *120*, 8144.
(2) Segale, D.; Karavitis, M.; Fredj, E.; Apkarian, V. A. *J. Chem. Phys.* **2005**, *122*, 111104.
(3) Stienkemeier, F.; Lehmann, K. K. *J. Phys. B* **2006**, *39*, R127.
(4) Karavitis, M.; Kumada, T.; Goldschleger, I. U.; Apkarian, V. A. *Phys. Chem. Chem. Phys.* **2005**, *7*, 791.
(5) Riga, J. M.; Fredj, E.; Martens, C. C. *J. Chem. Phys.* **2006**, *124*, 064506.
(6) Ma, Z.; Coker, D. F. *J. Chem. Phys.* **2008**, *128*, 244108.
(7) Billing, G. D. *The quantum classical theory*; Oxford University Press: Oxford, U.K., 2003.
(8) Horenko, I.; Salzmann, C.; Schmidt, B.; Schütte, C. *J. Chem. Phys.* **2002**, *117*, 11075.
(9) Horenko, I.; Weiser, M.; Schmidt, B.; Schütte, C. *J. Chem. Phys.* **2004**, *120*, 8913.
(10) Grossmann, F. *Comments At. Mol Phys.* **1999**, *34*, 141.
(11) Thoss, M.; Wang, H. *Annu. Rev. Phys. Chem.* **2004**, *55*, 299.
(12) Kay, Annu. *Rev. Phys. Chem* **2005**, *56*, 25.
(13) Heller, E. J. *J. Chem. Phys.* **1981**, *75*, 2923.
(14) Herman, M. F.; Kluk, E. *Chem. Phys.* **1984**, *91*, 27.
(15) Kay, K. G. *J. Chem. Phys.* **1994**, *100*, 4432.

(16) Kay, K. G. *J. Chem. Phys.* **1994**, *101*, 2250.
(17) Zhang, S.; Pollak, E. *Phys. Rev. Lett.* **2003**, *91*, 190201.
(18) Hochman, G.; Kay, K. G. *J. Phys. A* **2008**, *41*, 385303.
(19) Heller, E. J. *J. Chem. Phys.* **1975**, *62*, 1544.
(20) Deshpande, S. A.; Ezra, G. S. *J. Phys. A* **2006**, *39*, 5067.
(21) Grossmann, F. *J. Chem. Phys.* **2006**, *125*, 014111.
(22) Ovchinnikov, M.; Apkarian, V. A. *J. Chem. Phys.* **1996**, *105*, 10312.
(23) Guallar, V.; Batista, V. S.; Miller, W. H. *J. Chem. Phys.* **1999**, *110*, 9922.
(24) Zhang, S.; Pollak, E. *J. Chem. Phys.* **2004**, *121*, 3384.
(25) Goletz, C.-M.; Grossmann, F. *J. Chem. Phys.* **2009**, *130*, 244107.
(26) Goletz, C.-M.; Koch, W.; Grossmann, F. *Chem. Phys.* **2010**, *375*, 227.
(27) Gelabert, R.; Giménez, X.; Thoss, M.; Wang, H.; Miller, W. H. *J. Chem. Phys.* **2001**, *114*, 2572.
(28) Wang, H.; Thoss, M.; Sorge, K. L.; Gelabert, R.; Giménez, X.; Miller, W. H. *J. Chem. Phys.* **2001**, *114*, 2562.
(29) Herman, M. F. *J. Chem. Phys.* **1986**, *85*, 2069.
(30) Kluk, E.; Herman, M. F.; Davis, H. L. *J. Chem. Phys.* **1986**, *84*, 326.
(31) In the case of a non-Gaussian initial wave function, it can be decomposed to a given accuracy in terms of Gaussian wave packets.[47]
(32) Heller, E. J. In *Chaos et Physique Quantique/Chaos and Quantum Physics, Proc. Les Houches Summer School, Session LII (1989)*; Giannoni, M. J., Voros, A., Zinn-Justin, J., Eds.; North-Holland, Amsterdam: Amsterdam, 1991.
(33) Zadoyan, R.; Li, Z.; Martens, C. C.; Apkarian, V. A. *J. Chem. Phys.* **1994**, *101*, 6648.
(34) Bardeen, C. J.; et al. *J. Chem. Phys.* **1997**, *106*, 8486.
(35) Karavitis, M.; Apkarian, V. A. *J. Chem. Phys.* **2004**, *120*, 292.
(36) Segale, D.; Apkarian, V. A. *J. Chem. Phys.* **2011**, *135*, 024203.
(37) Ellison, F. O. *J. Am. Chem. Soc.* **1963**, *85*, 3540.
(38) Borowski, A.; Kühn, O. *J. Photochem. Photobiol.* **2007**, *190*, 169.
(39) Wilson, E. B.; Decius, J. C.; , Cross, P., *Molecular Vibrations*; McGraw-Hill: New York, 1955.
(40) Fleck, J. A.; Morris, J. R.; Feit, M. D. *App. Phys. A* **1976**, *10*, 129.
(41) Schmidt, B.; Lorenz, U. *Wavepacket 4.7.3: A program package for quantum-mechanical wavepacket propagation and time-dependent spectroscopy*; Available via http://wavepacket.sourceforge.net (2011).
(42) Schlosshauer, M. *Decoherence and Quantum-To-Classical Transition*; Springer: Berlin, 2007.
(43) Bergsma, J. P.; Berens, P. H.; Wilson, K. R.; Fredkin, D. R.; Heller, E. J. *J. Phys. Chem.* **1984**, *88*, 612.
(44) Wigner, E. *Phys. Rev.* **1932**, *40*, 749.
(45) In a similar manner, but starting from different initial conditions, non-Gaussian distortions are introduced in ref 48.
(46) Heller, E. J. *J. Chem. Phys.* **1976**, *65*, 1289.
(47) Horenko, I.; Schmidt, B.; Schütte, C. *J. Chem. Phys.* **2002**, *117*, 4643.
(48) Tomsovic, S.; Heller, E. J. *Phys. Rev. E* **1993**, *47*, 282.